nature energy

SUPPLEMENTARY INFORMATION

https://doi.org/10.1038/s41560-017-0071-2

In the format provided by the authors and unedited.

3D printing of shape-conformable thermoelectric materials using all-inorganic Bi_2Te_3-based inks

Fredrick Kim[1], Beomjin Kwon[2], Youngho Eom[1], Ji Eun Lee[3], Sangmin Park[1], Seungki Jo[1], Sung Hoon Park[1], Bong-Seo Kim[3], Hye Jin Im[3], Min Ho Lee[3], Tae Sik Min[4], Kyung Tae Kim[4], Han Gi Chae[1], William P. King[2] and Jae Sung Son[1]*

[1]School of Materials Science and Engineering, Ulsan National Institute of Science and Technology (UNIST), Ulsan, Republic of Korea. [2]Department of Mechanical Science and Engineering, University of Illinois Urbana-Champaign, Urbana, IL, USA. [3]Thermoelectric Conversion Research Center, Korea Electrotechnology Research Institute, Changwon, Republic of Korea. [4]Powder Technology Department, Korea Institute of Materials Science, Changwon, Republic of Korea. Fredrick Kim and Beomjin Kwon contributed equally to this work *e-mail: jsson@unist.ac.kr

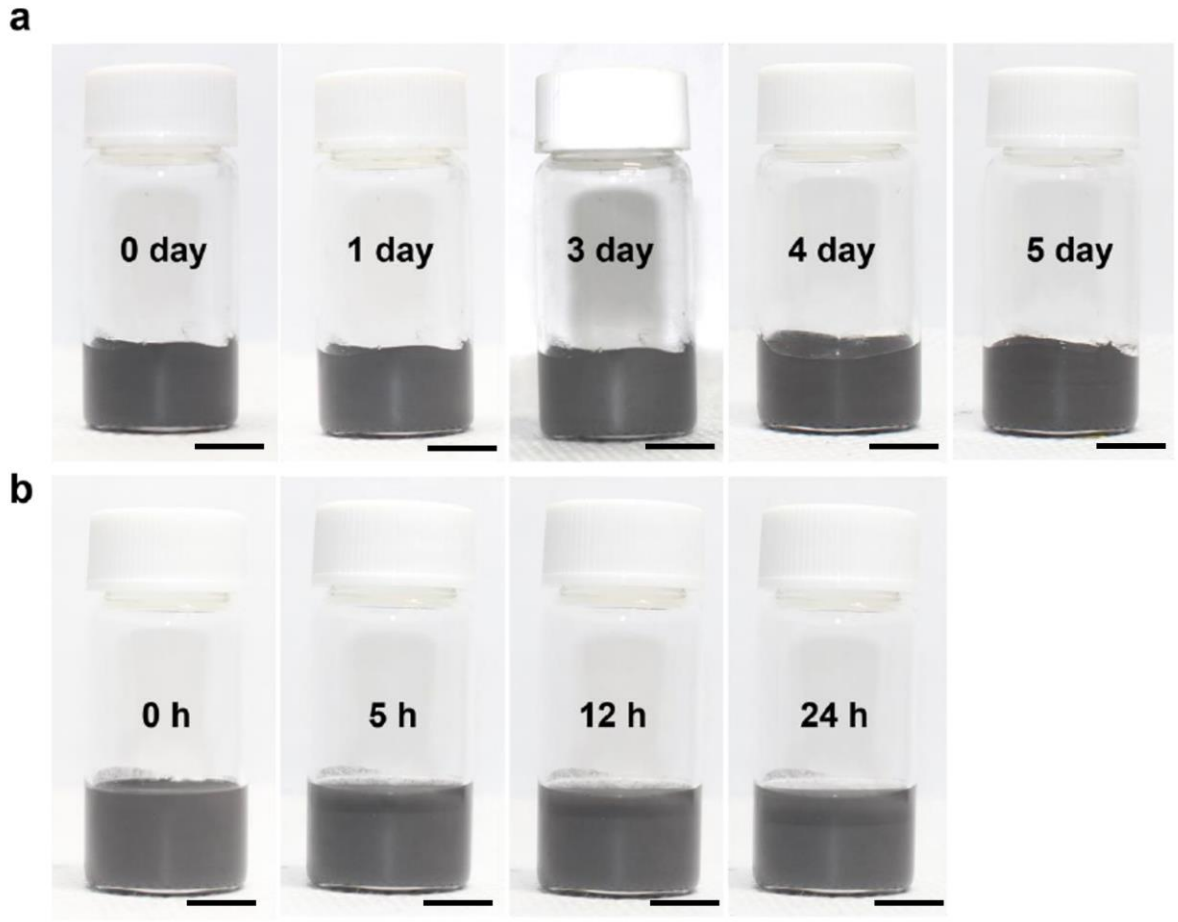

Supplementary Figure 1 | Dispersion stability of the TE inks. Time evolution of photographs showing the TE inks of (**a**) BST100/ChaM25 and (**b**) BST100/ChaM0. The sedimentation of TE ink without the ChaM took place within several hours after dispersion, but that of the TE ink containing the ChaM was delayed for more than four days. All scale bars correspond to 10 mm.

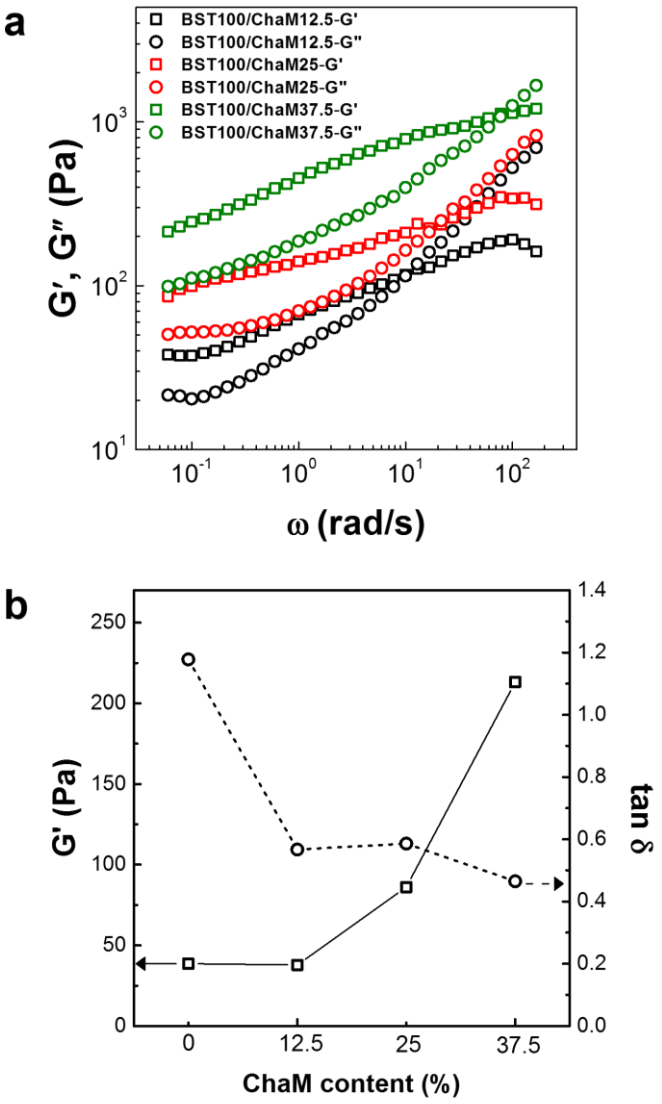

Supplementary Figure 2 | Rheological properties of TE inks. (**a**) The storage (G') and loss (G") moduli curves of the TE inks at 25 ºC. (**b**) Variation of the storage modulus (G') and loss tangent (tan δ) values at 0.05 rad/s with the content of the ChaM in the TE ink. The S_R values in Fig. 1e were obtained from the ratio of G' to 2G" at 0.05 rad/s.

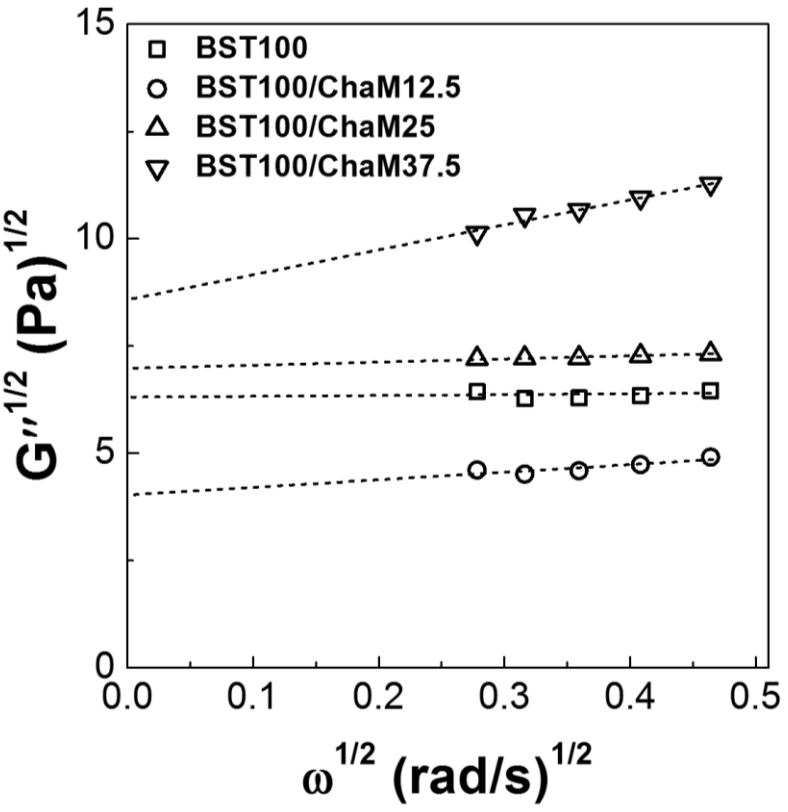

Supplementary Figure 3 | Casson plots of the TE ink with the ChaM contents of 12.5, 25 and 37.5%, respectively, at 25 °C. The τ_y values in Fig. 1e were obtained from the y-axis intercept of the Casson plot. The dashed lines indicate the extrapolation of the $G''^{1/2}$ curves.

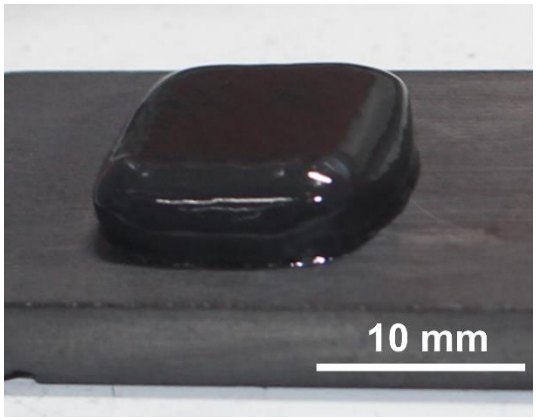

Supplementary Figure 4 | A photograph showing the as-printed sample before drying from the TE ink with 10 wt% of the ChaM.

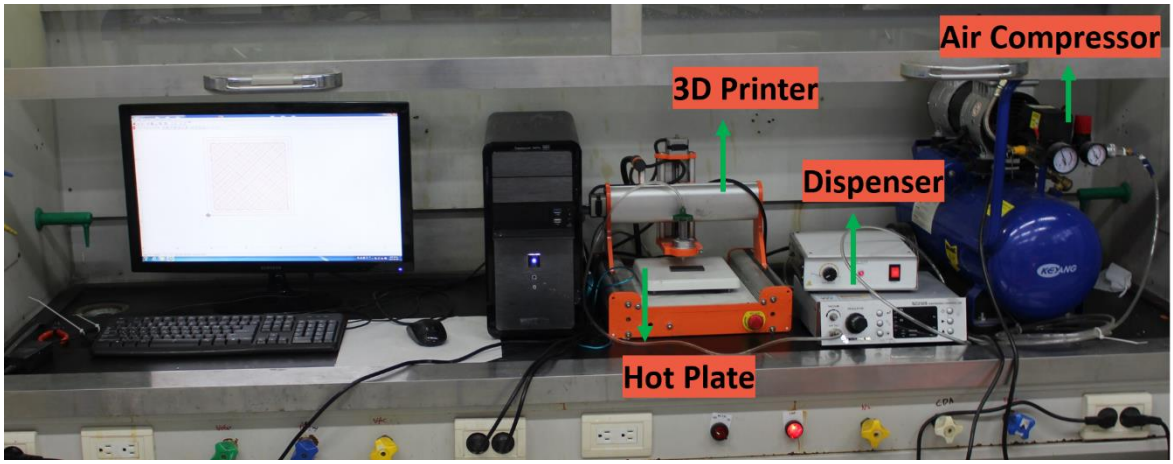

Supplementary Figure 5 | A photograph of the extrusion-based 3D printing equipment by an air-powered fluid dispenser.

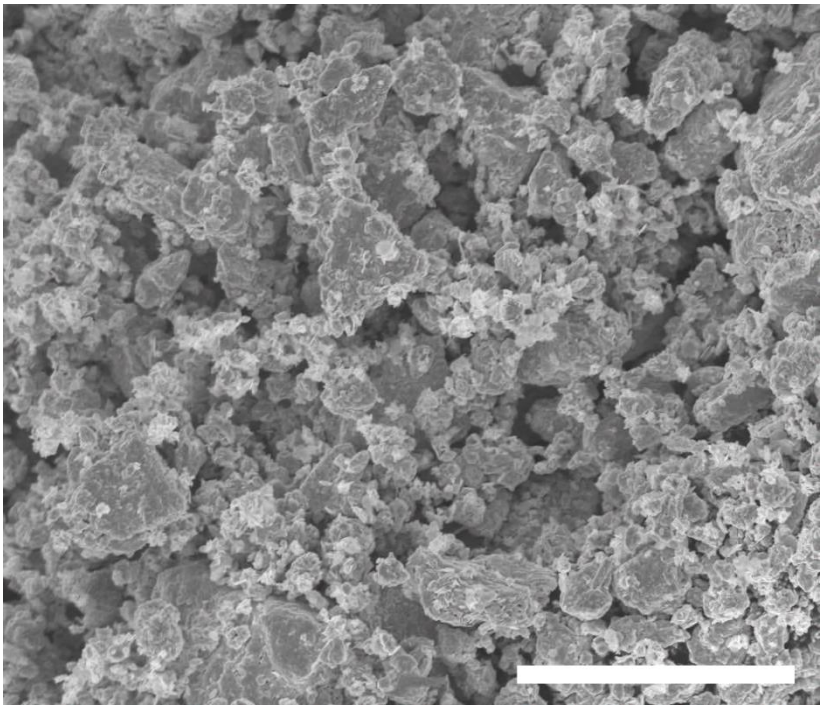

Supplementary Figure 6 | SEM image of the n-type 3D-printed TE materials upon drying at 105 °C. Scale bar corresponds to 10 µm.

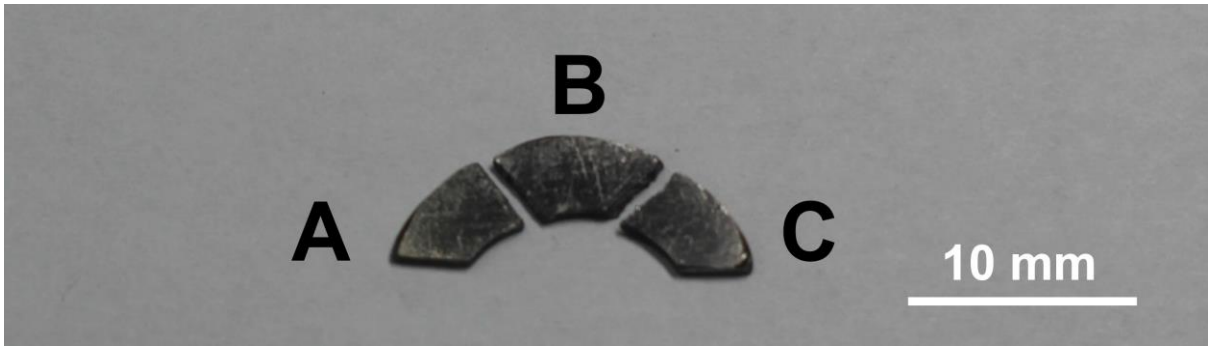

Supplementary Figure 7 | Three different pieces cut from the same half-ring for measuring TE properties.

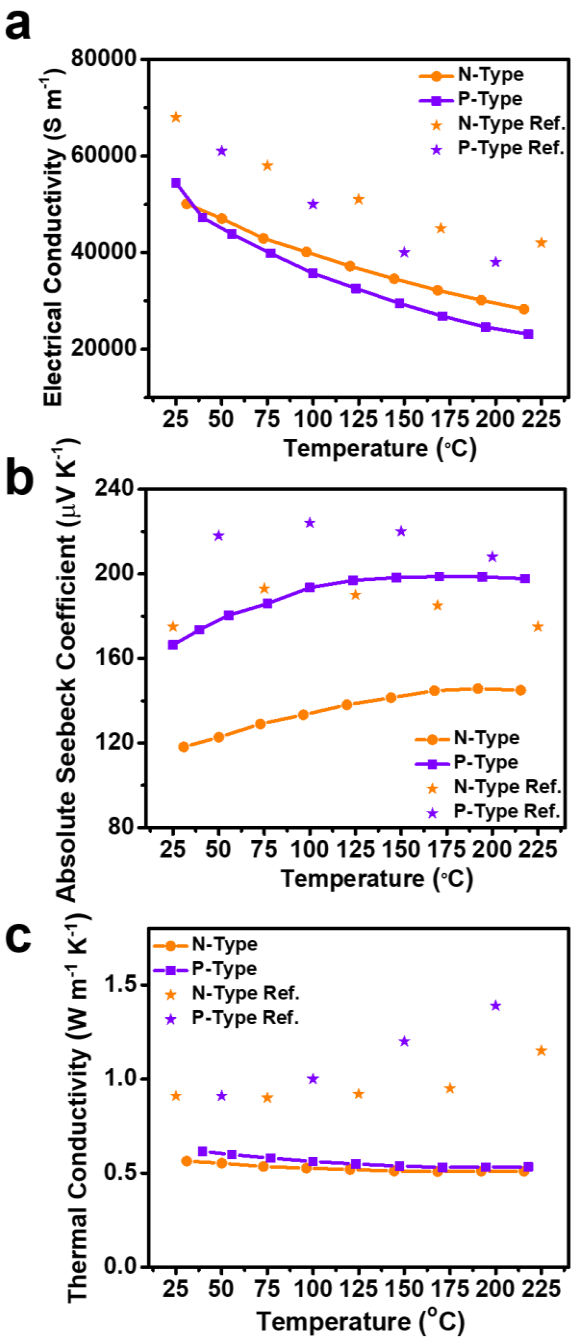

Supplementary Figure 8 | Comparison of TE properties of the 3D printed samples with the hot-pressed ones with corresponding compositions (**a**) Electrical conductivity, (**b**) Seebeck coefficient, and (**c**) thermal conductivity. The stars in panel (**c**) indicate data points obtained from the hot-pressed $Bi_{2.0}Te_{2.7}Se_{0.3}$[1] and $Bi_{0.4}Sb_{1.6}Te_{3.0}$[2].

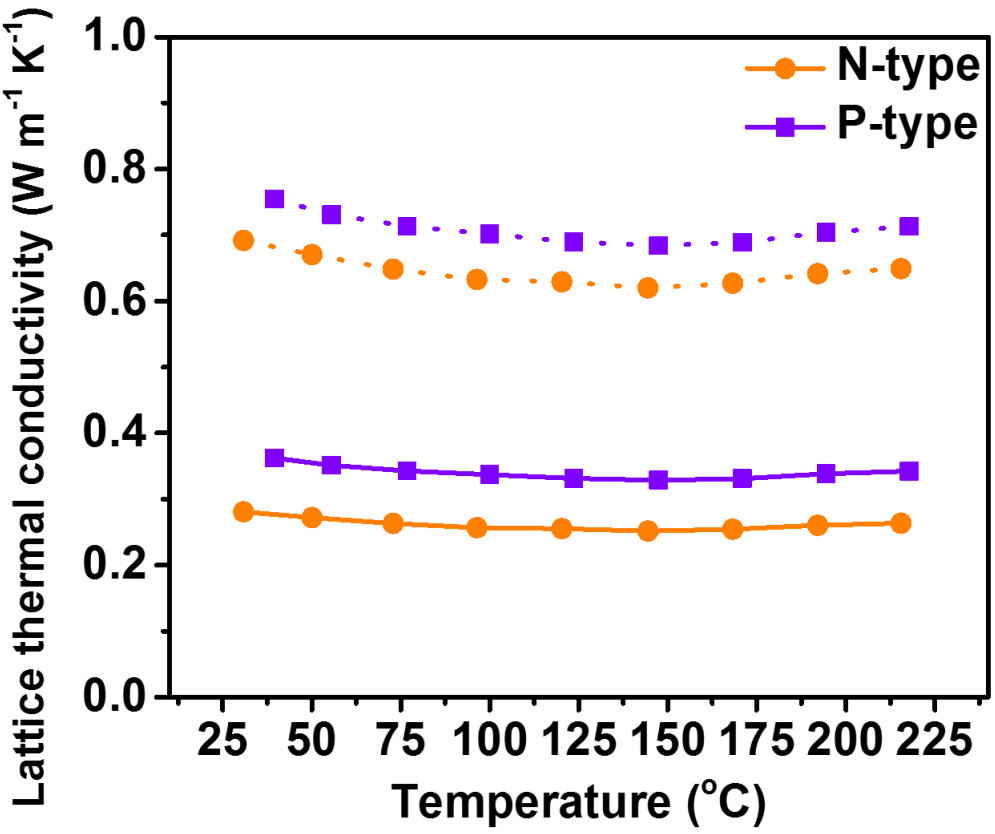

Supplementary Figure 9 | Lattice thermal conductivities of the n-type and p-type 3D printed samples and corrected lattice thermal conductivities using the modified formulation of the effective medium theory (dotted lines).

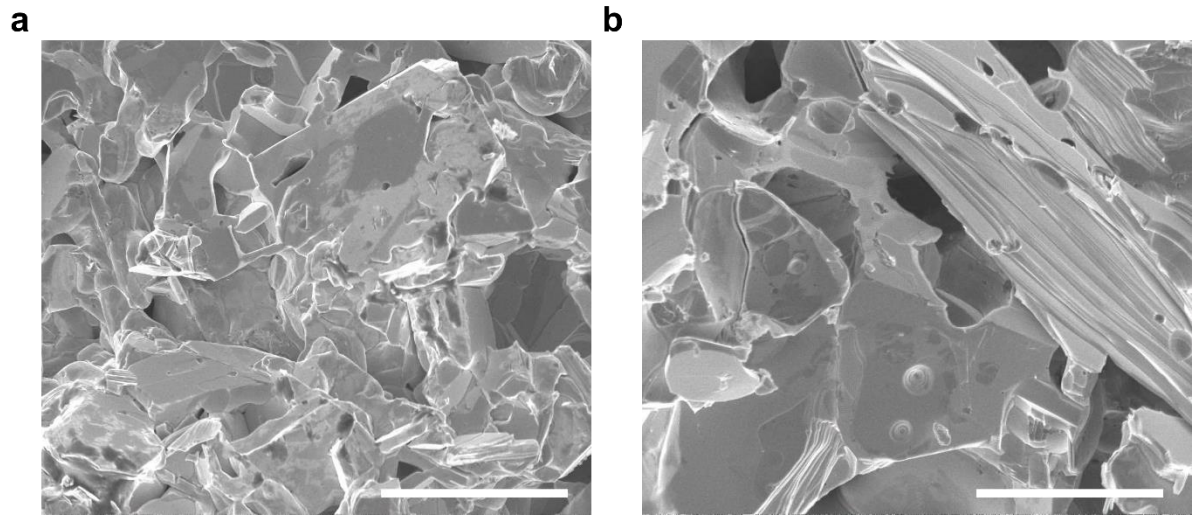

Supplementary Figure 10 | SEM images of fractured surfaces of (a) n-type and (b) p-type 3D-printed TE materials annealed at 450 °C. Scale bar corresponds to 10 μm.

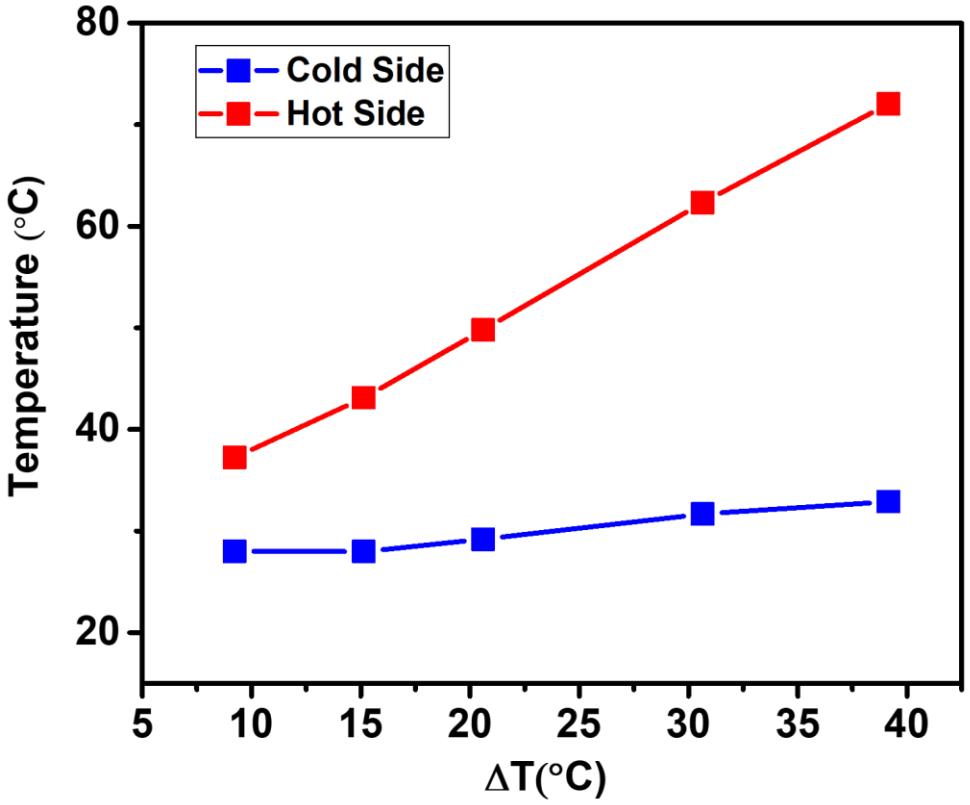

Supplementary Figure 11 | Temperatures on the hot and cold sides of the cylindrical TEG under a flow of hot water.

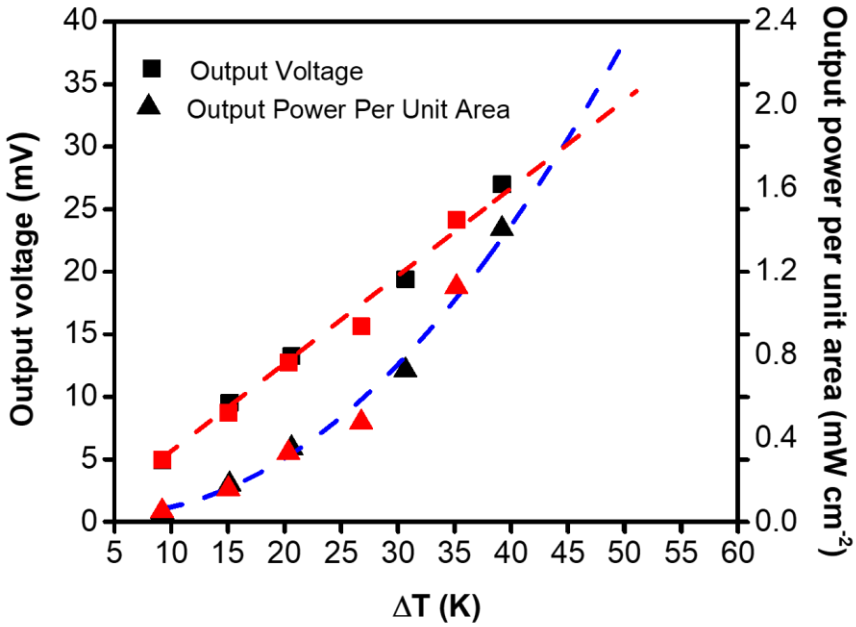

Supplementary Figure 12 | Output voltage and power density of the conformal cylindrical TEG as a function of a temperature difference. Black and red symbols indicate data points obtained from TEG#1 and TEG#2, respectively.

Supplementary Table 1. **Comparison of TE properties between the current p-type 3D printed sample and the previous reports[3] near room temperature.**

	Electrical conductivity ($S\ m^{-1}$)	Seebeck coefficient ($\mu V\ K^{-1}$)	Thermal conductivity ($W \cdot m^{-1} \cdot K^{-1}$)	ZT
This study	54462	166	0.616	0.75
Ref. B1	4800	148	0.26	0.12

Supplementary Table 2. The calculated Curzon-Ahlborn efficiency (η_{CA}) and Carnot efficiency (η_{Carnot}).

T_c (°C)	T_h (°C)	T_c/T_h	η_{CA}	η_{Carnot}
30	40	0.968	0.016	0.032
30	70	0.883	0.060	0.117

Supplementary Discussion

Rheological properties of all-inorganic TE inks.

The inks were prepared by the dispersion of the Sb_2Te_3-based ChaM binders in a suspension of $Bi_2Te_{2.7}Se_{0.3}$ (for n-type) or $Bi_{0.4}Sb_{1.6}Te_{3.0}$ (for p-type) TE particles in glycerol, followed by homogenization. The inks with different ChaM contents are hereafter referred to as BST100/ChaM#, where ChaM# is the ChaM content expressed as weight percentage of the ChaM binders to that of BiSbTe particles. Fig. 1e shows the dynamic viscosity (η') of the inks with ChaM contents of 0, 12.5, 25, and 37.5%. At low ChaM concentrations, the dynamic viscosity of the TE ink (BST100/ChaM12.5) was lower than that of BST100/ChaM0 over the whole frequency range. This suggests that adding a small amount of the ChaM binders induced a localised aggregation of the charged BiSbTe particles, thus reducing their effective volume (Fig. 1d). However, further addition of the ChaM (contents higher than 25%) increased η'. BST100/ChaM37.5 showed the highest η' of all samples over the measured frequency range, suggesting that the aggregates consisting of the charged BiSbTe particles experienced a stronger electrostatic interaction for higher ChaM contents (Fig. 1d). The phase stability of the specimens was evaluated from the loss tangent (tan δ) curves (Fig. 1f). An increase in tan δ indicates liquid-like behaviour of the specimen, while a decrease in this value indicates solid-like behaviour. It is interesting to note that the tan δ value of the TE inks containing the ChaM was below 1 in the lower frequency region and gradually increased with increasing frequency. Furthermore, a continuous decrease in tan δ was observed with increasing the ChaM content, suggesting that the behaviour of the TE ink became more solid-like and its colloidal stability was improved. On the other hand, BST100/ChaM0 yielded a tan δ value of 1.2 at 0.05 rad/s and showed shear-dependent behaviour, which implies that the BST particles with no ChaM formed a liquid-like structure with poor colloidal stability. Accordingly, the ink with no ChaM

frequently clogged the nozzle during printing. Further, BST100/ChaM25 displayed a greater storage modulus (G') but lower tan δ values than BST100/ChaM0 (Supplementary Fig. 2), demonstrating that the electrostatic binding effect of the ChaM improved the elasticity of the colloids, leading to higher colloidal stability.

The strength and elastic behaviours of the TE inks can be quantitatively assessed by the yield stress (τ_y) and recoverable elastic strain (S_R), as shown in Fig. 1g, which represent the minimum energy to break down the physical structure and the extent of elastic recovery, respectively. The τ_y and S_R values were obtained from the y-axis intercept of the Casson plot shown in Supplementary Fig. 3 and the ratio of G' to 2G" at 0.05 rad/s, respectively. As shown in Fig. 1g, the τ_y value of BST100 was 39.5 Pa, while that of BST100/ChaM25 was 49.4 Pa. On the other hand, the S_R value of BST100/ChaM25 was 0.85, which is more than two times higher than that of BST100/ChaM0 (0.41). The positive τ_y value but low viscoelasticity of BST100/ChaM0 ink indicates that the internal structure is dominantly driven by simple packing of the TE particles. Such dispersion states accelerate the sedimentation of the TE ink by gravitational force. However, the high viscoelasticity (increased τ_y and S_R) achieved by adding the ChaM suggests that TE particles establish the pseudo-network structure through the electrostatic interactions (Fig. 1d). Therefore, the ChaM-containing TE inks would show better structural integrity upon printing than ChaM-free TE inks. This high elastic strain achieved by TE inks with the ChaM binders satisfies the desired viscoelastic behaviour of inks for an extrusion-based 3D printing process.

The lattice thermal conductivity of the 3D printed materials

To further understand the thermal properties of the 3D printed samples, the lattice thermal conductivity (κ_L) of these samples was calculated by subtracting the electronic contribution of thermal conductivity (κ_E) from the total thermal conductivity, where κ_E was calculated by the Wiedemann-Franz Law, $\kappa_E=L_0\sigma T$, where L_0 is the Lorenz number, σ is the electrical conductivity and T is the absolute temperature[S1]. Also, L_0 was estimated by the equation based on the single parabolic band (SPB) model reported by Kim, *et al*.[4] The calculated values of κ_L of n-type and p-type samples ranges from 0.28 W m^{-1} K^{-1} to 0.36 W m^{-1} K^{-1} (Supplementary Fig. 9), which are slightly lower than the theoretically predicted lowest limit of the lattice thermal conductivity of Bi_2Te_3-based materials (0.21 W m^{-1} K^{-1})[5].

These ultralow thermal properties can be understood by considering the porosity of the 3D printed materials. Our group reported the paintable TE materials in that the painted and sintered TE layers exhibited the even lower lattice thermal conductivity that the currently 3D printed materials[6]. The painted materials had the multi-scale pores in nano- and macro-scales, which effectively scatter phonons in a broad range of wavelength to reduce the lattice thermal conductivity. Meanwhile, the macro-scale pores less affected the electrical carrier transport due to the relatively short mean free path of electron and hole carriers[7]. Likewise, the current 3D printed and sintered TE materials also possess the macro-scale pores to scatter phonons (Supplementary Fig. 10), responsible for the low lattice thermal conductivity. Also, the relatively high carrier mobility of the 3D printed TE materials further supported the existence of macro-scale pores.

To quantitatively understand the porosity effect on the κ_L, the κ_L of the n-type and p-type 3D printed samples were applied to the modified formulation of the effective medium theory equation of $\boldsymbol{\kappa_L = \kappa_h \frac{(2-2\Phi)}{(2+\Phi)}}$ suggested by Lee, *et al.*[7], where κ_h and Φ are the lattice thermal

conductivity of host materials and the porosity, respectively, The estimated κ_L were 0.62 W m^{-1} K^{-1} for the n-type sample and 0.68 W m^{-1} K^{-1} for the p-type sample (Supplementary Fig. 9), which were in the similar range of those observed in the nanostructured thermoelectric Bi_2Te_3 and BiSbTe materials[8].

Supplementary References

1. Suganuma, K. & Jiu, J. Advanced Bonding Technology Based on Nano- and Micro-metal Pastes, 2nd edition (ed. Lu, D. & Wong, C. P.) 589-626 (Springer, 2009)
2. Xue-Dong, L. & Park, Y.-H. Structure and transport properties of $(Bi_{1-x}Sb_x)_2Te_3$ thermoelectric materials prepared by mechanical alloying and pulse discharge sintering. *Mater. Trans.* **43**, 681–687 (2002).
3. He, M. *et al.* 3D Printing fabrication of amorphous thermoelectric materials with ultralow thermal conductivity. *Small* **11**, 5889-5894 (2015).
4. Kim, H.S., Gibbs, Tang, Y., Wang, H., & Snyder, G. J. Characterization of Lorenz number with Seebeck coefficient measurement. *APL Mater*. **3,** 041506 (2015).
5. Chiritescu, C., Mortensen, C., Cahill, D. G., Johnson, D. & Zschack, P. Lower limit to the lattice thermal conductivity of nanostructured Bi2Te3-based materials. *J. Appl. Phys*. **106**, 073503 (2009).
6. Park, S. H. *et al.* High-performance shape-engineerable thermoelectric painting. *Nat. Commun.* **7**, 13403 (2016).
7. Lee, H. et al. Effects of nanoscale porosity on thermoelectric properties of SiGe. *J. Appl. Phys*. **107**, 094308 (2010).
8. Mun, H., Choi, S. M., Lee, K. H. & Kim, S. W. Boundary engineering for the thermoelectric performance of bulk alloys based on bismuth telluride. *ChemSusChem* **8**, 2312-2326 (2015).